PHYSICAL REVIEW E **92**, 053016 (2015)

Model of heap formation in vibrated gravitational suspensions

Hiroyuki Ebata* and Masaki Sano†

Department of Physics, Graduate School of Sciences, Kyushu University, Fukuoka 812-8581, Japan

(Received 8 July 2015; revised manuscript received 19 October 2015; published 23 November 2015)

In vertically vibrated dense suspensions, several localized structures have been discovered, such as heaps, stable holes, expanding holes, and replicating holes. Because an inclined free fluid surface is difficult to maintain because of gravitational pressure, the mechanism of those structures is not understood intuitively. In this paper, as a candidate for the driving mechanism, we focus on the boundary condition on a solid wall: the slip-nonslip switching boundary condition in synchronization with vertical vibration. By applying the lubrication approximation, we derived the time evolution equation of the fluid thickness from the Oldroyd-B fluid model. In our model we show that the initially flat fluid layer becomes unstable in a subcritical manner, and heaps and convectional flow appear. The obtained results are consistent with those observed experimentally. We also find that heaps climb a slope when the bottom is slightly inclined. We show that viscoelasticity enhances heap formation and climbing of a heap on the slope.

DOI: 10.1103/PhysRevE.92.053016 PACS number(s): 47.54.−r, 45.70.Qj, 47.57.E−, 83.50.Rp

I. INTRODUCTION

Instability and pattern formation on the free surface of a fluid have long attracted the interest of physicists. The capillary force drives the Plateau-Rayleigh instability, in which a falling stream of fluid breaks up into smaller packets [1]. When a droplet is suspended in the air by an external force, a capillary wave is excited and gives the droplet a polygonal shape [2–4]. A denser fluid on a lighter fluid shows Rayleigh-Taylor instabilities [5]. Impulsive acceleration produces the Richtmyer-Meshkov instability [6,7]. Faraday found the Faraday wave, which is a resonance of the free surface wave to an external vibration [8]. Flow and surface instabilities induced by vibration are also studied with the objective of microfluidics and industrial applications [9–13]. Due to surface acoustic waves on solid boundaries, thin liquid film is drawn from a sessile droplet, and fingering instability and a solitonlike wave appear on that film [11].

Even if we focus on a Newtonian fluid, pattern formation on the free surface includes highly nonlinear and complex problems, and many researchers are working on them. When we use complex fluids that contain structures made from microscopic components, deformation and relaxation of the structure yield additional effects, and various new instabilities are reported [14].

In vertically vibrated dense suspensions, instabilities with an inclined free surface are found, such as heaps, stable holes, expanding holes, and replicating holes [15–22]. When we study the mechanism of these instabilities, we easily find that an intuitive understanding of the mechanism is inadequate. An inclined free fluid surface is generally difficult to maintain because surface deformation is suppressed by gravity. Thus, heaps and holes must resist gravitational pressure to maintain stable structures. Some nontrivial mechanism should convert the energy input by vertical vibration into a horizontal driving force. Similar surface instability and localized structures are also found in vibrated viscoplastic fluids and emulsions [23–25]. Because we cannot observe these phenomena in Newtonian fluids, it is important to identify the rheological features that are crucial for such surface instabilities.

In this study, we propose a model of heaps in a vibrated non-density-matched suspension (gravitational suspension) [26]. Heaps are investigated in both vibrated dry granular materials [27–33] and vibrated wet granules [34,35]. In both cases, the granules are completely immersed in the fluid. Thus, the free surface is not taken into account. In the presence of less interstitial liquid, called the capillary state [15], many granules stay at the liquid-air interface, and we have to consider the effect of the free surface. In this case, as we mentioned before, the most crucial problem is how to maintain steady deformation of the free surface under gravity. As a candidate for the driving mechanism, we propose a slip boundary condition at a solid wall [26]. In addition to the bulk rheological characteristics, such as the yield stress, shear thinning, and shear thickening, dense suspensions also have a specific boundary condition at a solid wall [36–38]. If the shear stress at the wall τ_w is sufficiently small, dense suspensions stick to the solid boundary. When τ_w exceeds a critical value, dense suspensions slip on the wall. In our model, we assume that τ_w is a function of gravity, and a boundary condition shows slip-nonslip switching in synchronization with vertical vibration. By applying the lubrication approximation, the time evolution equation of the fluid thickness is derived.

Under the slip-nonslip switching boundary condition, we show that the initially flat fluid layer becomes unstable, and heaps and convectional flow appear. This surface instability was shown to be analogous to Rayleigh-Taylor instability [39–42]. From a weak nonlinear analysis, we show that subcritical pitchfork bifurcation always occurs for a viscous fluid. These features are consistent with results reported experimentally [15]. In this paper, viscoelasticity is introduced to the model proposed in our previous work [26]. In a viscoelastic fluid, if the relaxation time of the shear stress is small, almost all the features resemble those of a viscous fluid. When the relaxation time exceeds a critical value, the dynamics of the heaps changes crucially. In addition, we found that heaps can climb a slope, and viscoelasticity enhances the climbing.

*ebata@phys.kyushu-u.ac.jp

†Also at Department of Physics, Graduate School of Science, The University of Tokyo, Tokyo 113-0033, Japan; sano@phys.s.u-tokyo.ac.jp

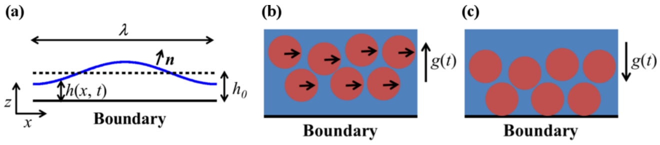

FIG. 1. (Color online) (a) Schematic illustration of the system. (b, c) Schematic illustration of the boundary condition. (b) When $g(t) > 0$, granules slip on the bottom. (c) When $g(t) < 0$, granules stick on the bottom.

The validity of the model is examined with the experiment on the drift motion of a heap.

II. MODEL EQUATIONS

First, we introduce the governing equations of the model [26]. We consider a fluid layer with thickness $h(x,t)$ on a solid bottom plate [Fig. 1(a)]. A mixture of granules and interstitial fluid is treated as a single fluid, with velocity v_i, pressure p, and a deviatoric stress τ_{ij}. Vertical vibration is represented by oscillating gravity as $g(t) = -g[1 - \Gamma \sin(\omega t)]$, where Γ and ω are the normalized vibration acceleration and vibration frequency, respectively. The conservation of linear momentum is

$$\rho \frac{Dv_i}{Dt} = -\frac{\partial p}{\partial x_i} + \frac{\partial \tau_{ij}}{\partial x_j} - \frac{\partial \phi}{\partial x_i}, \tag{1}$$

$$\phi = \rho g[1 - \Gamma \sin(\omega t)]z, \tag{2}$$

where ϕ is the gravity potential. Compared to the compressibility of dry granular media, that of a suspension is reduced by the drag force of the interstitial liquid and a capillary force. Thus, we assume incompressibility and uniformity of the packing fraction in our model, $\partial_{x_i} v_i = 0$.

When the gravitational suspension is vertically vibrated, even very weak vibration causes the loss of yield stress, and a viscosity plateau appears at a low shear rate [43]. Thus, we do not consider the yield stress. Recently, a rheological model of vibrated granular suspension was proposed [44,45]. They also tested the model through experiments. That proposed equation in Ref. [45] consists of a Maxwell-Jeffreys model with two nonlinear terms. Since only single shear rate is considered, this model is an equation of scalar variable. When we extend this model to tensor form, it appears to be a special case of Oldroyd 8 constant fluid. For simplicity, we neglect the nonlinear elasticity and use an Oldroyd B constitutive equation in this paper,

$$\tau_{ij} + \lambda_1 \overset{\triangledown}{\tau}_{ij} = 2\eta(D_{ij} + \lambda_2 \overset{\triangledown}{D}_{ij}), \tag{3}$$

$$D_{ij} = \frac{1}{2}\left(\frac{\partial v_i}{\partial x_j} + \frac{\partial v_j}{\partial x_i}\right), \tag{4}$$

where λ_1 and λ_2 are the relaxation time and retardation time, respectively. The overhead symbol $\triangledown$ represents the upper convected time derivative. For example, the upper convected time derivative of a variable X is

$$\overset{\triangledown}{X}_{ij} = \partial_t X_{ij} + v_k \frac{\partial X_{ij}}{\partial x_k} - \frac{\partial v_i}{\partial x_k} X_{kj} - \frac{\partial v_j}{\partial x_k} X_{ik}. \tag{5}$$

If $\lambda_2 = 0$, Eq. (3) corresponds to the Maxwell model.

The kinematic boundary condition and force balance condition at the free surface (at $z = h$) are

$$\partial_t h + v_x \partial_x h + v_y \partial_y h = v_z, \tag{6}$$

$$(-p\delta_{ij} + \tau_{ij})n_j = -\kappa \sigma n_i, \tag{7}$$

where n_i is the unit outward vector normal to the surface, κ is the curvature of the surface, and σ is the surface tension [Fig. 1(a)]. In the two-dimensional (2D) case, $\mathbf{n} = (n_x, n_z)$ and κ has the form

$$\mathbf{n} = \frac{(-\partial_x h,\ 1)}{(1 + (\partial_x h)^2)^{1/2}}, \quad \kappa = \frac{\partial_x^2 h}{(1 + (\partial_x h)^2)^{3/2}}. \tag{8}$$

In this paper, we consider the case that the granules are surrounded by the interstitial fluid as in the experiment of Ref. [15]. When the packing fraction of the granules is 45%–60%, the granular layer is completely covered with a free surface of interstitial fluid. Thus, we used the surface tension of the interstitial fluid as that of the suspension.

When we consider the steady shear of an ordinary Newtonian fluid such as water or oil, we generally adopt a nonslip condition at a solid boundary. However, dense suspensions reportedly can slip along a solid boundary depending on the shear stress [36–38]. Dense suspensions stick to a solid boundary if the shear stress is sufficiently small but can slip if the shear stress exceeds a critical value. If we use a step function $\theta(x)$, the slip boundary conditions at $z = 0$ are

$$v_z = 0, \tag{9}$$

$$v_i - \frac{\beta_0}{\eta_w}\tau_{iz}\left(1 - \frac{\tau_c}{\tau}\right)\theta(\tau - \tau_c) = 0, \tag{10}$$

where $\tau = \sqrt{\tau_{xz}^2 + \tau_{yz}^2}$, $i \in (x,y)$, and

$$\theta(x) = \begin{cases} 1 & (x \geqslant 0) \\ 0 & (x < 0) \end{cases}. \tag{11}$$

In Eq. (10), we set the second term to zero at $\tau = 0$. η_w and τ_c are the viscosity of the interstitial fluid and the critical shear stress above which slip occurs, respectively [37]. β_0 is called the slip length, which has a length dimension.

In heaping experiments, granules are generally chosen to be heavier than the surrounding fluid. In a non-density-matched suspension, when gravity $g(t)$ acts downward, granules are pushed to the bottom. On the other hand, when gravity $g(t)$ acts upward, granules are released from the bottom. Here, we introduce an important assumption [26]. If the granules are pushed to the bottom, τ_c becomes large, and if the granules are released from the bottom, τ_c becomes small. We assume that τ_c is an increasing function of $g(t)$. For convenience, we introduce a modified slip length β:

$$\beta = \beta_0\left(1 - \frac{\tau_c[g(t)]}{\tau}\right)\theta(\tau - \tau_c[g(t)]). \tag{12}$$

To make the analysis easier, we use the condition that τ_c becomes sufficiently large compared to shear stress when $g(t) < 0$, and τ_c is 0 when $g(t) > 0$ [Figs. 1(b) and 1(c)].

The boundary condition, Eq. (10), can be simplified as

$$v_i - \frac{\beta}{\eta_w}\tau_{iz} = 0, \tag{13}$$

$$\beta = \beta_0\theta[g(t)]. \tag{14}$$

This boundary condition is crucial for our model, which switches between slip and nonslip conditions in synchronization with vertical vibration. In Eq. (14), we assume that the granular layer touches the bottom plate when gravity acts downward. However, at high vibration frequency, the motion of the granular layer could have a phase delay. The necessary condition for Eq. (14) is estimated in Appendix A.

III. LUBRICATION APPROXIMATION

To avoid solving the full three-dimensional fluid equations, we apply a lubrication approximation. In the experiment, the typical size of heaps near the critical acceleration corresponds to the size of the container. The depth of the fluid layer is $\sim$1.0 cm and the size of the container is $\sim$10 cm. Thus, the aspect ratio is $\sim$0.1. In the model, the validity of the lubrication approximation is ensured if the wavelength of the instability is much larger than the depth of the fluid.

By applying a lubrication approximation, we seek to construct an equation for the evolution of the fluid layer thickness $h(x,t)$. Here, we introduce two length scales [42]. One is the mean thickness of the fluid h_0, and the other is the length scale in the horizontal direction determined by the wavelength λ, which should be larger than h_0. We define a small parameter ϵ as

$$\epsilon = \frac{2\pi h_0}{\lambda}. \tag{15}$$

It is natural to scale z to h_0 and x to h_0/ϵ, which is equivalent to λ. The normalized coordinates are

$$Z = \frac{z}{h_0}, \qquad X = \frac{\epsilon x}{h_0}. \tag{16}$$

We choose a typical velocity U_0 in the x direction as a characteristic velocity of the system. Because the dominant driving force is gravity in our model, we set $U_0 = \epsilon\rho g h_0^2/\eta$, which is the typical velocity of a spreading and dewetting fluid film. If we require continuity for a dimensionless fluid equation, the normalized velocity should have the form

$$U = \frac{u}{U_0}, \qquad W = \frac{w}{\epsilon U_0}. \tag{17}$$

There are two time scales in this case. The slower time scale is $\lambda/U_0 \sim h_0/(\epsilon U_0)$. This corresponds to the time scale of formation and relaxation of a heap (typically, several seconds). On the other hand, the faster time scale is the cycle of vibration $2\pi/\omega \sim 0.01$ s. This is much faster than the time scale of heap formation. Because we seek to know how the surface becomes unstable with vibration, we choose the faster time scale as that of the model. We define the scaled time and the corresponding time derivative as

$$T = \omega t, \quad \partial_T = \frac{1}{\omega}\partial_t. \tag{18}$$

We assume that the gradients of the shear stress and pressure are the dominant terms of the motion equation in the horizontal direction. This can be expressed as $-\partial_x p \sim \partial_z\tau_{xz}$. Thus, the normalized pressure and stress are defined as

$$P = \frac{\epsilon h_0}{\eta U_0}p, \qquad \Sigma_{ij} = \frac{h_0}{\eta U_0}\tau_{ij}. \tag{19}$$

The normalized gravity and surface tension have the forms

$$G = \frac{\epsilon\rho h_0^2}{\eta U_0}g, \qquad C^{-1} = \frac{\epsilon^3\sigma}{U_0\eta}. \tag{20}$$

Further, h and β are scaled as

$$H = \frac{h(x_i,t)}{h_0}, \qquad \bar{\beta} = \frac{\beta}{h_0}. \tag{21}$$

The system has the following nondimensional numbers:

$$\mathrm{Re} = \frac{h_0 U_0}{\epsilon\nu}, \quad \mathrm{St} = \frac{\omega h_0}{\epsilon U_0}, \tag{22}$$

$$\mathrm{De}_1 = \omega\lambda_1, \quad \mathrm{De}_2 = \omega\lambda_2, \tag{23}$$

$$\mathrm{We} = \lambda_1\frac{U_0}{h_0}, \quad \mathrm{We}_2 = \lambda_2\frac{U_0}{h_0}, \tag{24}$$

where Re and St are the Reynolds number and Strouhal number, respectively, De_1 and De_2 are the Deborah numbers, and We_1 and We_2 are the Weissenberg numbers. The scaled motion equation is obtained as follows:

$$\begin{aligned}&\epsilon^2\mathrm{ReSt}\partial_T U + \epsilon^2\mathrm{Re}\,(U\partial_X U + W\partial_Z U)\\ &\quad= -\partial_X P + \epsilon\partial_X\Sigma_{xx} + \partial_Z\Sigma_{xz},\end{aligned} \tag{25}$$

$$\begin{aligned}&\epsilon^3\mathrm{ReSt}\partial_T W + \epsilon^3\mathrm{Re}\,(U\partial_X W + W\partial_Z W)\\ &\quad= -\partial_Z P + \epsilon^2\partial_X\Sigma_{xz} + \epsilon\partial_Z\Sigma_{zz} + G(T),\end{aligned} \tag{26}$$

where $G(T) = -G[1 - \Gamma\sin(T)]$, and $\nu = \eta/\rho$. Because a dense suspension has a high viscosity, the system should be strongly dissipative. Thus, we introduce Stokes' approximation here [46]. We assume $\epsilon^2\mathrm{ReSt} = \omega h_0^2/\nu \ll 1$. Then we ignore the inertia term in Eqs. (25) and (26):

$$0 = -\partial_X P + \epsilon\partial_X\Sigma_{xx} + \partial_Z\Sigma_{xz}, \tag{27}$$

$$0 = -\partial_Z P + \epsilon^2\partial_X\Sigma_{xz} + \epsilon\partial_Z\Sigma_{zz} + G(T). \tag{28}$$

The normalized continuity equation is

$$\partial_X U + \partial_Z W = 0. \tag{29}$$

The normalized constitutive equations are

$$\tilde{\mathbf{L}}_1\Sigma_{xx} - 2\mathrm{We}_1\Sigma_{xz}\partial_Z U = -2\mathrm{We}_2(\partial_Z U)^2 + O(\epsilon), \tag{30}$$

$$\tilde{\mathbf{L}}_1\Sigma_{zz} = O(\epsilon), \tag{31}$$

$$\tilde{\mathbf{L}}_1\Sigma_{xz} - \mathrm{We}_1\Sigma_{zz}\partial_Z U = \tilde{\mathbf{L}}_2\partial_Z U + O(\epsilon), \tag{32}$$

where we introduce the following operator:

$$\tilde{\mathbf{L}}_1 = 1 + \mathrm{De}_1\partial_T, \quad \tilde{\mathbf{L}}_2 = 1 + \mathrm{De}_2\partial_T. \tag{33}$$

The exact forms of the normalized constitutive equations are shown in Appendix B. The boundary conditions are scaled as follows. At $Z = H$,

$$-P - \epsilon^2 \Sigma_{xz}\partial_X H + \epsilon \Sigma_{zz} = \frac{C^{-1}\partial_X^2 H}{[1+\epsilon^2(\partial_X H)^2]^{3/2}}, \quad (34)$$

$$[1-\epsilon^2(\partial_X H)^2]\Sigma_{xz} + \epsilon \partial_X H(\Sigma_{zz} - \Sigma_{xx}) = 0, \quad (35)$$

$$\partial_T H + \frac{1}{\mathrm{St}}\partial_X \int_0^H U dZ = 0, \quad (36)$$

where we use a continuity equation to obtain Eq. (36). At $Z = 0$,

$$W = 0, \quad U - \bar{\beta}\frac{\Sigma_{xz}}{\eta_{w0}} = 0, \quad (37)$$

where $\eta_{w0} = \eta_w/\eta$ is the normalized viscosity of the interstitial fluid. By using the definition $U_0 = \epsilon \rho g h_0^2/\eta$,

$$G = 1, \quad C^{-1} = \frac{\epsilon^2\sigma}{\rho g h_0^2}, \quad \mathrm{St} = \frac{\omega\nu}{\epsilon^2 g h_0}. \quad (38)$$

The driving forces of this system are gravity and surface tension, so we let $C = O(1)$ as $\epsilon \to 0$. The term $1/\mathrm{St}$ has the order $O(\epsilon^2)$. However, because we aim to obtain the time evolution equation of H, we do not neglect $1/\mathrm{St}$ in Eq. (36). At the leading order of ϵ, the following equations are obtained from Eqs. (27)–(37). The scaled motion equation is

$$0 = -\partial_X P + \partial_Z \Sigma_{xz}, \quad (39)$$

$$0 = -\partial_Z P + G(T). \quad (40)$$

The scaled constitutive equations are

$$\tilde{\mathbf{L}}_1\Sigma_{xx} - 2\mathrm{We}_1\Sigma_{xz}\partial_Z U = -2\mathrm{We}_2(\partial_Z U)^2, \quad (41)$$

$$\tilde{\mathbf{L}}_1\Sigma_{zz} = 0, \quad (42)$$

$$\tilde{\mathbf{L}}_1\Sigma_{xz} - \mathrm{We}_1\Sigma_{zz}\partial_Z U = \tilde{\mathbf{L}}_2\partial_Z U. \quad (43)$$

Further, at $Z = H$,

$$-P = C^{-1}\partial_X^2 H, \quad (44)$$

$$\Sigma_{xz} = 0, \quad (45)$$

$$\partial_T H + \frac{1}{\mathrm{St}}\partial_X \int_0^H U dZ = 0. \quad (46)$$

And, at $Z = 0$,

$$W = 0, \qquad U - \bar{\beta}\frac{\Sigma_{xz}}{\eta_{w0}} = 0. \quad (47)$$

To simplify the equations, we introduce a reduced pressure:

$$\bar{P} = -\left[G(T) + C^{-1}\partial_X^2\right]H. \quad (48)$$

By using $\bar{P}$, the pressure and shear stress are obtained from Eqs. (39) and (40):

$$P = G(T)Z + \bar{P}, \quad (49)$$

$$\Sigma_{xz} = \partial_X \bar{P}(Z - H). \quad (50)$$

From Eq. (42), Σ_{zz} is solved as $\Sigma_{zz} = \Sigma_{zz}(0)\exp(-t/\mathrm{De})$. This solution of Σ_{zz} indicates that only the initial perturbation relaxes to zero. Thus, we assume $\Sigma_{zz} = 0$. Then Eq. (43) gives

$$U = \int_0^Z dZ' \tilde{\mathbf{L}}_2^{-1}\tilde{\mathbf{L}}_1\Sigma_{xz}, \quad (51)$$

where $\tilde{\mathbf{L}}_2^{-1}$ is the inverse operator of $\tilde{\mathbf{L}}_2$,

$$\tilde{\mathbf{L}}_2^{-1}f(t) = \frac{e^{t/\mathrm{De}_2}}{\mathrm{De}_2}\int_0^t dt' f(t')e^{-t'/\mathrm{De}_2}, \quad (52)$$

where $f(t)$ is a given function. Because the shear stress Σ_{xz} is solved in Eq. (50), the velocity U can be calculated from Eq. (51). W can also be obtained by solving the continuity equation, Eq. (29):

$$U = \frac{1}{2}\tilde{\mathbf{L}}_2^{-1}\tilde{\mathbf{L}}_1(\partial_X\bar{P})Z^2 - \tilde{\mathbf{L}}_2^{-1}\tilde{\mathbf{L}}_1(H\partial_X\bar{P})Z - \frac{\bar{\beta}}{\eta_{w0}}H\partial_X\bar{P}, \quad (53)$$

$$W = -\partial_X\left\{\frac{1}{6}\tilde{\mathbf{L}}_2^{-1}\tilde{\mathbf{L}}_1(\partial_X\bar{P})Z^3 - \frac{1}{2}\tilde{\mathbf{L}}_2^{-1}\tilde{\mathbf{L}}_1(H\partial_X\bar{P})Z^2 - \frac{\bar{\beta}}{\eta_{w0}}H\partial_X\bar{P}Z\right\}. \quad (54)$$

By substituting U in Eq. (46), we obtain the evolution equation of H:

$$\partial_T H + \frac{1}{\mathrm{St}}\partial_X\left\{\frac{1}{6}H^3\tilde{\mathbf{L}}_2^{-1}\tilde{\mathbf{L}}_1\partial_X\bar{P} - \frac{1}{2}H^2\tilde{\mathbf{L}}_2^{-1}\tilde{\mathbf{L}}_1(H\partial_X\bar{P}) - \frac{\bar{\beta}}{\eta_{w0}}H^2\partial_X\bar{P}\right\} = 0. \quad (55)$$

The dimensional form of the time evolution equation is

$$\eta\partial_t h + \partial_x\left\{\frac{1}{6}h^3\mathbf{L}_2^{-1}\mathbf{L}_1\partial_x\bar{p} - \frac{1}{2}h^2\mathbf{L}_2^{-1}\mathbf{L}_1(h\partial_x\bar{p}) - \frac{\beta\eta}{\eta_w}h^2\partial_x\bar{p}\right\} = 0, \quad (56)$$

where $\mathbf{L}_j = 1 + \lambda_j\partial_t$, $j = 1,2$. By using Eq. (52) and the partial integral, the following relation is obtained:

$$\mathbf{L}_2^{-1}\mathbf{L}_1 f(t) = \frac{\lambda_1}{\lambda_2}f(t) + \left(1 - \frac{\lambda_1}{\lambda_2}\right)\mathbf{L}_2^{-1}f(t) + \frac{\lambda_1}{\lambda_2}e^{-t/\lambda_2}f(0), \quad (57)$$

where $f(t)$ is a given function. Then Eq. (56) can be transformed as follows:

$$\eta\partial_t h = \partial_x\left\{\left(1 - \frac{\lambda_1}{\lambda_2}\right)\left(-\frac{1}{6}h^3\mathbf{L}_2^{-1}\partial_x\bar{p} + \frac{1}{2}h^2\mathbf{L}_2^{-1}(h\partial_x\bar{p})\right) + \left(\frac{\lambda_1}{3\lambda_2}h + \frac{\beta\eta}{\eta_w}\right)h^2\partial_x\bar{p} + \frac{\lambda_1}{\lambda_2}e^{-t/\lambda_2}X_0\right\}, \quad (58)$$

$$X_0 = \tfrac{1}{6}h^3[\partial_x\bar{p}]_{t=0} - \tfrac{1}{2}h^2[h\partial_x\bar{p}]_{t=0}. \quad (59)$$

The above equation does not have a time derivative term on the right-hand side. Thus, in the numerical simulation, we use Eq. (58).

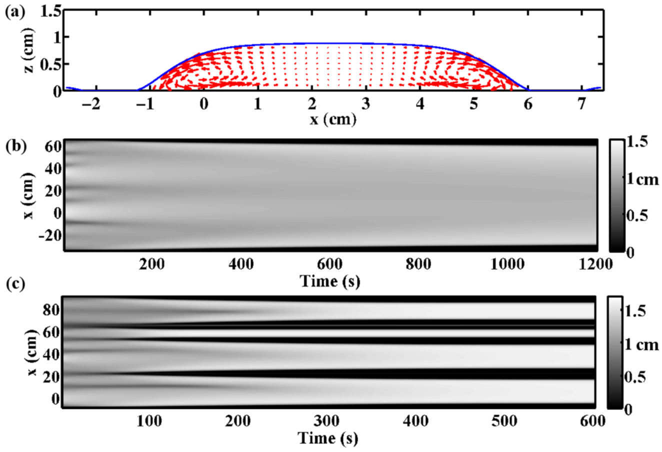

FIG. 2. (Color online) (a) Heap in steady state (blue line) and time-averaged velocity field (red arrows). (b, c) Spatiotemporal plot of heaps. Horizontal and vertical axes are time and position, respectively. Gray scale represents the height of $h(x,y)$. A brighter region indicates greater height (see color bar). (b) $\Gamma = 2.2$. (c) $\Gamma = 2.41$. (a–c) $\eta = 100$ St, $\sigma = 72$ dyne/cm, $f = 10$ Hz, $h_0 = \beta_0\eta/\eta_w = 0.5$ cm. We use a disjoining pressure. See Appendix C. (a) $B = 10\,000$ Pa, $h_p = 0.005$ cm. (b, c) $B = 10$ Pa, $h_p = 0.005$ cm. (a–c) Initial condition is $h(x,y) = h_0 + \xi_0 \sum_{n=1}^{n=m} \sin(2\pi nx/L + \phi_n)$. L is the system size. ϕ_n is a random number uniformly distributed from 0 to 2π. (a) $\xi_0 = 0.01$ cm, $L = 10$ cm, $m = 5$. (b, c) $\xi_0 = 0.05$ cm, $L = 100$ cm, $m = 10$.

A. Newtonian fluid

For a 2D Newtonian fluid, the time evolution equation is derived by setting $\lambda_1 = \lambda_2 = 0$ in Eq. (56) [26]:

$$\eta\partial_t h = \partial_x\left\{\left(\frac{1}{3}h + \frac{\eta}{\eta_w}\beta_0\theta[g(t)]\right)h^2\partial_x\bar{p}\right\}, \tag{60}$$

$$\bar{p} = -\left[\rho g(t) + \sigma\partial_x^2\right]h. \tag{61}$$

We simulate Eq. (60) with a periodic boundary condition. When the acceleration Γ is sufficiently large, the flat surface becomes unstable and a steady deformation grows to form heaps [Figs. 2(a)–2(c)]. When the acceleration exceeds a critical value, the valley of the heaps reaches the bottom plate and the fluid layer shows a rupture. Therefore, ultimately, heaps are separated by a dry region. Near the critical acceleration, the size of a heap is comparable to that of the system [Figs. 2(a) and 2(b)]. The shape of the heap is slightly modulated by vibration, but the positions of the peak and the bottom of the surface do not change during one vibration cycle. As the acceleration increases, higher wave numbers become unstable and the size of the heap decreases [Fig. 2(c)]. The time-averaged behavior of heaps shows convectionlike flow [Fig. 2(a)]. The flow moves upward at the peak of the deformation and then downward from the peak. We also found that the onset acceleration is independent of the vibration frequency and shows hysteresis. These results are consistent with experimental observations of heaping [15].

We check the bifurcation type of a viscous fluid by a weak nonlinear analysis. Here, we use a model equation for a viscous fluid proposed in Ref. [26]:

$$\partial_t h = -\partial_x\left\{\int_0^h dz\int_0^z dz'\frac{\tau_{xz}(z')}{\eta[\tau_{xz}(z')]} + \beta\frac{\tau_{xz}(0)}{\eta_w}h\right\},$$
$$\tau_{xz} = (h-z)\left[\rho g(t) + \sigma\partial_x^2\right]\partial_x h, \tag{62}$$

where $\eta(\tau_{xz})$ could be a function of the shear stress τ_{xz}, and we set $\eta(\tau_{xz} = 0) = \eta_0$. We assume the periodic boundary condition in the x direction.

First, we calculate the linear stability of the evolution equation. We linearize Eq. (62) at $h = h_0$ and calculate the time-averaged growth rate Λ_k defined by $h_k(T) = \exp(\Lambda_k T)h_k(0)$:

$$\Lambda_k = \frac{1}{T}\int_0^T dt\frac{k^2}{\eta_0}\left(\frac{1}{3}h_0^3 + \frac{\eta_0}{\eta_w}\beta h_0^2\right)[\rho g(t) - \sigma k^2]$$
$$= \frac{\beta_0 h_0^2\rho g k^2}{2\pi\eta_w}\left\{-\left[\frac{2\pi h_0\eta_w}{3\beta_0\eta_0} + \pi - 2\sin^{-1}\left(\frac{1}{\Gamma}\right)\right]\right.$$
$$\left.\times\left(1 + \frac{\sigma}{\rho g}k^2\right) + 2\sqrt{\Gamma^2 - 1}\right\}, \tag{63}$$

where k is the wave number, and T is a cycle of the vibration. Λ_k has the same functional form as Rayleigh-Taylor instability in a thin film [39–42]. In an infinitely large system, the onset acceleration Γ_{c0} satisfies

$$-\pi + 2\sin^{-1}\left(\frac{1}{\Gamma_{c0}}\right) + 2\sqrt{\Gamma_{c0}^2 - 1} = \frac{2\pi h_0\eta_w}{3\beta_0\eta_0}. \tag{64}$$

This onset acceleration is independent of the vibration frequency and depends only on $\eta_0\beta_0/(h_0\eta_w)$. This condition of onset acceleration has the same form as that in Ref. [15].

Next, we consider the case in which the acceleration differs slightly from the onset acceleration:

$$\Gamma = \Gamma_c + \epsilon_2^2\chi\Gamma_c, \quad \epsilon_2 = \sqrt{\frac{|\Gamma - \Gamma_c|}{\Gamma_c}}, \tag{65}$$

where χ is the sign of $\Gamma - \Gamma_c$, and ϵ_2 is a small parameter. We assume that only one wave number, k_m, which corresponds to the system size, has neutral stability and the other wave numbers are sufficiently stable. When k_m is too small, huge numbers of harmonics nk_m are very close to neutral stability. In this case we cannot neglect higher harmonics [47]. To ignore the higher harmonics of k_m, ϵ_2 should be smaller than $k_m h_0$. Therefore, we do not treat too-small values of k_m, and we assume that $k_m h_0$ is around 0.1. Then we expand h in a perturbation series in powers of ϵ_2:

$$h = h_0 + \epsilon_2 h_1 + \epsilon_2^2 h_2 + \cdots. \tag{66}$$

Next, we expand the viscosity $\eta^{-1}(\tau_{xz})$ in powers of ϵ_2. Owing to the spatial symmetry, the viscosity $\eta(\tau_{xz})$ is an even function of τ_{xz}. Therefore, the inverse of the viscosity is expanded as

$$\eta^{-1}(\tau_{xz}) = \eta_0^{-1} - \epsilon_2^2\eta_0^{-2}\frac{\partial^2\eta(0)}{\partial\tau_{xz}^2}(\tau_{xz1})^2\ldots, \tag{67}$$

$$\tau_{xz1} = (h_0 - z)\left[\rho g_c(t) + \sigma\partial_x^2\right]\partial_x h_1, \tag{68}$$

$$g_c(t) = g[-1 + \Gamma_c\sin(\omega t)], \tag{69}$$

where τ_{xz1} is the shear stress of $O(\epsilon_2)$. To simplify the equations, we replace $\eta_0\beta/\eta_w$ with β. First, we introduce the following operator:

$$\mathbf{L}_0 = \partial_t + \eta_0^{-1}\left(\frac{1}{3}h_0^3 + \beta h_0^2\right)\left[\rho g_c(t) + \sigma\partial_x^2\right]\partial_x^2. \quad (70)$$

Then the equation in $O(\epsilon_2)$ is

$$\mathbf{L}_0 h_1 = 0. \quad (71)$$

From the assumption, the neutral stable solution can be written as

$$h_1 = A\hat{h}_1(t)\exp(ik_m x) + \text{c.c.}, \quad (72)$$

where A has a complex value, and we set $\hat{h}_1(0) = 1$. Because the acceleration differs slightly from the onset acceleration, the amplitude A evolves very slowly. The time scale τ of A is $O(\epsilon_2^2)$, and we introduce the slow time scale $\tau = \epsilon_2^2 t$. Thus, the time derivative should be transformed as

$$\partial_t \to \partial_t + \epsilon_2^2\partial_\tau. \quad (73)$$

The equation in $O(\epsilon_2^2)$ becomes

$$\mathbf{L}_0 h_2 = -\eta_0^{-1}\partial_x\left\{\left(h_0^2 + 2\beta h_0\right)h_1\left(\rho g_c(t) + \sigma\partial_x^2\right)\partial_x h_1\right\}. \quad (74)$$

The specific solution of h_2 can be written as

$$h_2 = A^2\hat{h}_2(t)\exp(2ik_m x) + \text{c.c.} \quad (75)$$

Finally, the equation in $O(\epsilon_2^3)$ becomes

$$\mathbf{L}_0 h_3 = M. \quad (76)$$

The explicit forms of h_1,h_2, and M are derived in Appendix D. The solvability condition requires that M is orthogonal to $\hat{h}_1$,

$$\frac{1}{T}\int_0^T dt\hat{h}_1^{-1}M = 0. \quad (77)$$

Then we obtain the evolution equation of A,

$$\partial_\tau A = \alpha A + \gamma A|A|^2, \quad (78)$$

where the explicit forms of α and γ are shown in Appendix D. Henceforth, we calculate γ at the leading order in k_m. Here, we use the following relation:

$$\Gamma_c = \Gamma_{c0} + O\left(k_m^2\right), \quad (79)$$

where Γ_{c0} is the onset acceleration at $k_m = 0$ [see Eq. (64)]. Further, h_1 and h_2 are constant at the leading order in k_m,

$$\hat{h}_1 = 1 + O\left(k_m^2\right), \quad (80)$$

$$\hat{h}_2 = \frac{\rho g}{6\sigma h_0}\frac{F_2}{F_1}k_m^{-2} + O(1), \quad (81)$$

where F_1 and F_2 are defined as follows:

$$F_1 = \frac{2\beta_0}{\pi h_0}\sqrt{\Gamma_{c0}^2 - 1}, \qquad F_2 = -\frac{2\pi}{3}. \quad (82)$$

By substituting Eqs. (80) and (81) into Eq. (D15), γ can be written as

$$\gamma = \frac{\rho^2 g^2 h_0}{12\pi\eta_0\sigma}\frac{F_2^2}{F_1} + O\left(k_m^2\right). \quad (83)$$

Because F_1 is positive, γ is always non-negative. Therefore, subcritical pitchfork bifurcation always occurs. Notice that γ does not depend on the non-Newtonian viscosity [Fig. 3(a)]. The unstable branch calculated from Eq. (78) collapses to that computed in the simulation [Fig. 3(b)]. Thus, without elasticity, the linear and weakly nonlinear regimes are completely determined by the slip-nonslip switching boundary condition.

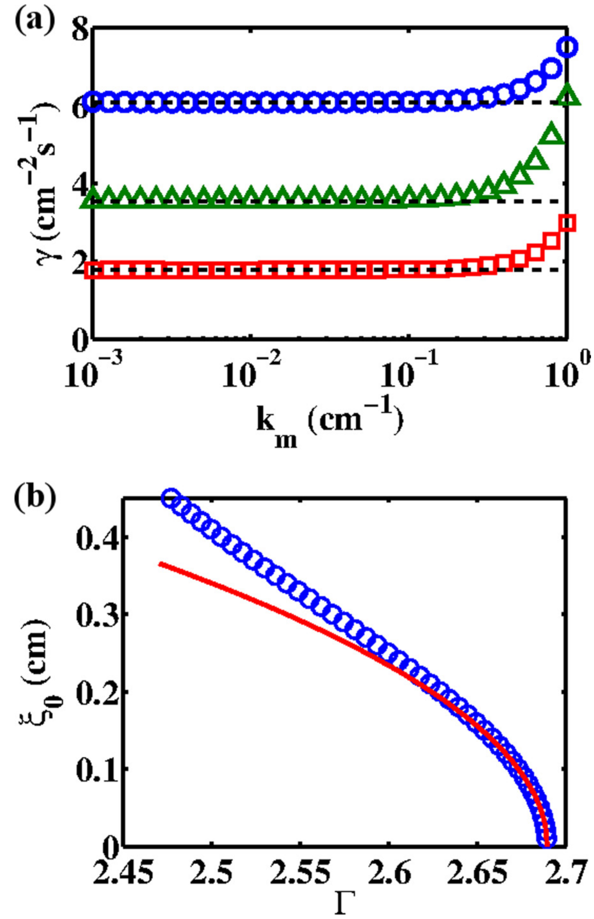

FIG. 3. (Color online) (a) Dependence of γ on k calculated from Eq. (D15). Dashed black line is calculated from Eq. (83). Blue circles: $\eta = 100$ St, and $\sigma = 21$ dyne/cm. Green triangles: $\eta = 50$ St, and $\sigma = 72$ dyne/cm. Red squares: $\eta = 100$ St, and $\sigma = 72$ dyne/cm. (b) Blue circles indicate unstable branch of Eq. (60) with periodic boundary condition in two dimensions. ξ_0 is the initial deformation, $h = h_0 + \xi_0\sin(k_m x)$. Above the symbol, the fluid layer ends in rupture. Below the symbol, the fluid layer relaxes to become flat. Red solid line is unstable branch calculated from Eq. (78). $\eta = 50$ St, and $\sigma = 72$ dyne/cm. (a, b) Parameter values are $k_m = 2\pi/5$ cm^{-1}, $f = 10$ Hz, $h_0 = \beta_0\eta/\eta_w = 0.5$ cm, and $\rho = 1$ g/cm^3.

B. Viscoelastic fluid

Here, we simulate the evolution equation of a viscoelastic fluid [Eq. (58)]. We assume $\lambda_1 > \lambda_2$ and change λ_1 to examine the effects of the elasticity. For small λ_1, the numerical result becomes similar to that for the Newtonian fluid. Above the critical acceleration, long wavelengths become unstable and heaps are formed. Once the heaps appear, the valleys of the heaps reach the bottom plate and a dried region appears. We also found hysteresis in heap formation. Compared to the

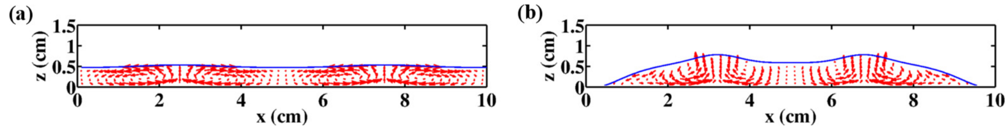

FIG. 4. (Color online) Bistable states of heaps in viscoelastic fluid. Blue curve indicates time-averaged surface, and red arrows indicate time-averaged velocity field. Relaxation time λ_1 is set to exceed a critical value λ_c. (a) Small initial surface deformation. Initial condition is $h(x,y) = h_0 - 0.05\cos(4\pi nx/L)$. $L = 10$ cm is the system size. (b) Large initial surface deformation. Initial condition is $h(x,y) = h_0 - 0.3\cos(2\pi nx/L)$. Parameter values are $\lambda_1 = 0.15$ s, $\Gamma = 2.37$, $\eta = 100$ St, $\sigma = 72$ dyne/cm, $h_0 = \beta\eta/\eta_w = 0.5$ cm, $\rho = 1$ g/cm^3, and $\lambda_2 = 0.01$ s. We use a disjoining pressure. See Appendix C. $B = 10$ Pa, $h_p = 0.005$ cm.

Newtonian fluid, the amplitude of the oscillation of the shape becomes large because of the shear thinning viscosity.

When λ_1 exceeds a critical relaxation time λ_c, heap formation changes crucially. Above λ_c, the most unstable wave number k_c has a finite value at the onset acceleration [Fig. 4(a)]. At the onset acceleration of the heap, wave number k_m, which corresponds to the system size, is also very close to neutral stability. Thus, we cannot neglect the growth of wave number k_m. We found that the bifurcation type depends on the wave number. As we measured, the heap of wave number k_c undergoes supercritical pitchfork bifurcation. On the other hand, the heap of wave number k_m undergoes subcritical pitchfork bifurcation. Thus, around the onset acceleration, the system shows a bistable state. If the initial deformation of the surface is sufficiently small, the amplitude of wave number k_c dominantly grows and the heaps with k_c reach the steady state [Fig. 4(a)]. In this case, the valleys of the heaps are shallow and a fluid layer always covers the bottom plate. If a large deformation with long wavelength is initially made, the amplitude of wave number k_m dominantly grows and the heaps with k_m reach the steady state [Fig. 4(b)]. In this case, the valleys of the heaps are deep and a dried region appears.

Next, we calculate the linear stability of a viscoelastic fluid. Equation (58) is linearized at $h = h_0$, and a Fourier transformation gives

$$\eta\mathbf{L}_2\partial_t\xi_k = \frac{k^2}{3}h_0^3\mathbf{L}_1\{[\rho g(t) - \sigma k^2]\xi_k\} + k^2\frac{\eta}{\eta_w}\mathbf{L}_2\{\beta h_0^2[\rho g(t) - \sigma k^2]\xi_k\}, \quad (84)$$

where ξ_k is a small deformation with wave number k. Using Floquet's theorem, we numerically calculate the time-averaged growth rates from Eq. (84). Equation (84) has two growth rates, and one of them always has a negative value. Here, we set the larger growth rate as Λ_k. The dependence of Λ_k on k at the onset acceleration is shown in Fig. 5(a). As λ_1 increases, Λ_k becomes flat at around $k = 0$. There exists a critical relaxation time $\lambda_1 = \lambda_c$ above which the critical wave number k_c has a finite value. Figures 5(b) and 5(c) show the onset acceleration and critical wave number, respectively, of a sufficiently large system (system size is 10^4 cm). For a very large system, below the critical relaxation time λ_c the onset acceleration and critical wave number are identical to those of a Newtonian fluid. Above λ_c, the critical wave number increases as $k_c \sim (\lambda_1 - \lambda_c)^{1/2}$ and the onset acceleration decreases.

Next, we estimate the critical relaxation time λ_c. For simplicity we consider only the case $\lambda_2 = 0$. Then the time-averaged growth rate Λ_k has the form

$$\Lambda_k = \frac{1}{T}\int_0^T dt\frac{k^2\left(\frac{1}{3}h_0^3 + \frac{\eta}{\eta_w}\beta h_0^2\right)[\rho g(t) - \sigma k^2]}{\eta - \lambda_1\frac{k^2}{3}h_0^3[\rho g(t) - \sigma k^2]}. \quad (85)$$

The analytical expression of Λ_k is rather complicated. Thus, we do not show it here. However, we note that the onset acceleration and critical wave number are independent of the frequency f. Henceforth, we consider an infinitely large system and assume that the critical wave number is sufficiently small around λ_c. Then only small k is considered, and we expand Λ_k in the series of k. Equation (85) contains only k^2 terms. Thus, Λ_k is a function of k^2,

$$\Lambda_k = \alpha_{k2}k^2 + \alpha_{k4}k^4 + \alpha_{k6}k^6 + \cdots. \quad (86)$$

We then calculate α_{k2},α_{k4}, and α_{k6}. α_{k2} is identical to that of a viscous fluid,

$$\alpha_{k2} = \lim_{k^2\to 0}\left(\frac{\Lambda_k}{k^2}\right) = \frac{\rho g}{\eta}(-B + A), \quad (87)$$

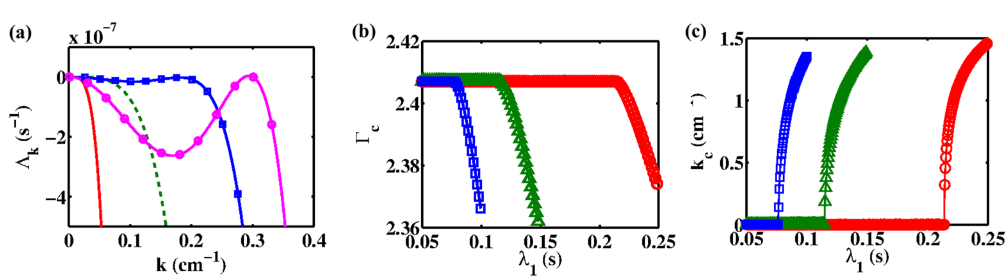

FIG. 5. (Color online) (a) Dependence of Λ_k on k at the critical acceleration Γ_c. $\lambda_2 = 0.01$ s. Red solid line: viscous fluid. Green dashed line: $\lambda_1 = 1.135 \times 10^{-1}$ s. Blue squares: $\lambda_1 = 1.150 \times 10^{-1}$ s. Magenta circles: $\lambda_1 = 1.155 \times 10^{-1}$ s. (b) Dependence of Γ_c on λ_1. Red circles: $\lambda_2 = 0.001$ s. Green triangles: $\lambda_2 = 0.01$ s. Blue squares: $\lambda_2 = 0.02$ s. (c) Dependence of k_c on λ_1. Red circles: $\lambda_2 = 0.001$ s. Green triangles: $\lambda_2 = 0.01$ s. Blue squares: $\lambda_2 = 0.02$ s. (a–c) Parameter values are $\eta = 100$ St, $\sigma = 72$ dyne/cm, $h_0 = \beta\eta/\eta_w = 0.5$ cm, and $\rho = 1$ g/cm^3.

where A and B are defined as follows:

$$A = \frac{\beta_0 h_0^2 \eta}{\pi \eta_w}\sqrt{\Gamma^2 - 1}, \tag{88}$$

$$B = \frac{1}{3}h_0^3 + \frac{\beta_0 h_0^2 \eta}{\eta_w}\left[\frac{1}{2} - \frac{1}{\pi}\sin^{-1}\left(\frac{1}{\Gamma}\right)\right], \tag{89}$$

and α_{k4} is calculated as follows:

$$\alpha_{k4} = \lim_{k^2\to 0}\frac{\partial}{\partial k^2}\left(\frac{\Lambda_k}{k^2}\right) = -B\frac{\sigma}{\eta} + \frac{\lambda_1 h_0^3}{3}\left(\frac{\rho g}{\eta}\right)^2\left\{\left(1+\frac{\Gamma^2}{2}\right)B - \frac{3}{2}A\right\}. \tag{90}$$

Similarly, α_{k6} is calculated as follows:

$$\alpha_{k6} = \frac{1}{2}\lim_{k^2\to 0}\frac{\partial^2}{\partial k^2 \partial k^2}\left(\frac{\Lambda_k}{k^2}\right) = -\frac{2}{3}(A-B)\frac{\lambda_1 \rho g \sigma}{\eta^2} + \frac{1}{9}\left\{\left(\frac{11}{6}+\frac{2}{3}\Gamma^2\right)A - \left(1+\frac{3}{2}\Gamma^2\right)B\right\}\lambda_1^2 h_0^6\left(\frac{\rho g}{\eta}\right)^3, \tag{91}$$

where α_{k2} is independent of λ_1, so λ_1 affects only α_{k4} and α_{k6}. For a viscous fluid, α_{k4} is always negative. Thus, for an infinitely large system, the condition $\alpha_{k2} = 0$ gives the onset acceleration. If α_{k4} becomes positive at $\alpha_{k2} = 0$, the onset acceleration should change and the critical wave number has a finite value. The condition $\alpha_{k4} > 0$ with $\alpha_{k2} = 0$ gives the critical relaxation time λ_c:

$$\lambda_1 > \lambda_c = \frac{6\sigma\eta}{\rho^2 g^2 h_0^3(\Gamma_{c0}^2 - 1)}, \tag{92}$$

where Γ_{c0} is the onset acceleration of a Newtonian fluid [Eq. (64)]. As shown in Fig. 6(a), λ_c calculated from Eq. (92) is in good agreement with λ_c directly computed from Eq. (85). If $\lambda_1 - \lambda_c$ is small and positive, the critical wave number k_c is given by $k_c^2 = \alpha_{k4}/(2\alpha_{k6})$. When we ignore the deviation of Γ_c from Γ_{c0}, k_c is written as

$$k_c^2 = \frac{9}{10}\frac{\eta}{\rho g \lambda_c^2 h_0^3}(\lambda_1 - \lambda_c) = \frac{1}{40}\frac{\rho^3 g^3 h_0^3}{\sigma^2 \eta}(\Gamma_{c0}^2 - 1)^2(\lambda_1 - \lambda_c). \tag{93}$$

We confirm this relation by numerical simulation [Fig. 6(b)]. For $\lambda_2 \neq 0$, λ_c is an increasing function of f and λ_2 [Fig. 6(c)]. If $k_c h_0 \ll 1$ is satisfied, the lubrication approximation is valid. From Eqs. (92) and (93), a large viscosity and small thickness of the fluid yield a large λ_c and small k_c. Therefore, for a highly viscous thin film, the lubrication approximation can be applied to a viscoelastic fluid having a large relaxation time.

IV. CLIMBING OF A HEAP

In this section, we focus on the dynamics of an isolated heap. First, we do not consider the elasticity, the effect of which is discussed later. We apply our model to the case in which the bottom plate is slightly inclined from the horizontal axis. In the model, the inclination of the bottom can be expressed by adding horizontal gravity $G_h(T)$ to Eq. (39). Therefore, we need only to modify the reduced pressure [Eq. (61)],

$$\bar{p} = -[\rho g(t) + \sigma(\partial_x^2 + \partial_y^2)]h - \rho g_h(t)x + \psi, \tag{94}$$

where we introduce the disjoining pressure ψ to treat the contact line (see Appendix C). The gravities are $g(t) = \cos\theta_b g[-1 + \Gamma\sin(\omega t)]$ and $g_h(t) = \sin\theta_b g[-1 + \Gamma\sin(\omega t)]$, where θ_b is the angle of inclination from the x axis. In the simulation, we apply a periodic boundary condition and place a heap as an initial condition. As shown in Figs. 7(a)–7(c), the heap starts to climb the slope as the acceleration increases. When $g(t)$ and $g_h(t)$ are both negative, the boundary condition on the bottom is nonslip. On the other hand, when both gravities are positive, the boundary condition on the bottom is slip. Therefore, it is easy for the heap to flow when the gravities are positive. Thus, a heap starts to climb the slope when the acceleration becomes sufficiently large. Climbing of a heap reminds us of vibration-induced climbing of a droplet [48], where it indicates the importance of a nonlinear friction law between the droplet and a bottom plate.

A time series of the velocity of the centroid V_g is shown in Fig. 7(d). For all the cases, V_g oscillates around a mean value. The oscillation comes from the contact line dynamics. The time average of V_g is shown in Fig. 7(e). As the acceleration increases, V_g monotonically increases. When the angle of the slope θ_b is small, the heap sometimes adheres to the bottom plate because of the force from the contact line. For $\theta_b = 0.5°$,

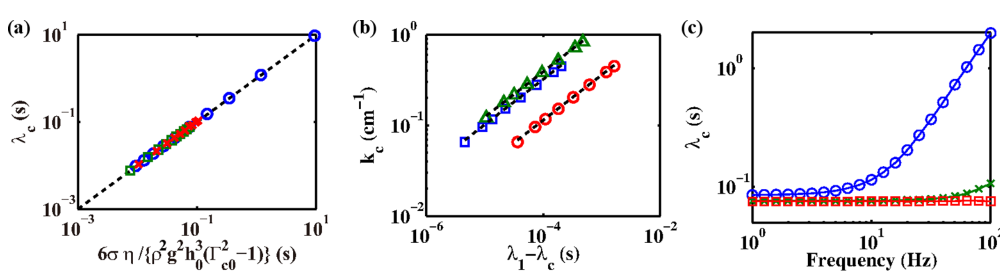

FIG. 6. (Color online) (a) Dependence of λ_c on parameter values. Horizontal and vertical axes are λ_c calculated from Eq. (92) and λ_c directly computed from Eq. (85), respectively. Blue circles: $\sigma = 72$ dyne/cm, $\eta = 100$ St. h_0 is varied from 0.1 to 1 cm. Green squares: $\sigma = 72$ dyne/cm, $h_0 = 0.5$ cm. η is varied from 10 St to 100 St. Red crosses: $\eta = 100$ St, $h_0 = 0.5$ cm. σ is varied from 10 dyne/cm to 100 dyne/cm. (b) Dependence of critical wave number k_c on λ_1 around λ_c. Black dashed line is calculated from Eq. (93). Blue squares: $h_0 = 1$ cm, $\sigma = 72$ dyne/cm. Green triangles: $h_0 = 0.5$ cm, $\sigma = 21$ dyne/cm. Red circles: $h_0 = 0.5$ cm, $\sigma = 72$ dyne/cm. η is fixed at 100 St. (c) Dependence of λ_c on frequency and λ_2. Red squares: $\lambda_2 = 0.000\,1$ s. Green crosses: $\lambda_2 = 0.001$ s. Blue circles: $\lambda_2 = 0.01$ s. Parameter values are $h_0 = 0.5$ cm, $\sigma = 72$ dyne/cm, $\eta = 100$ St. (a, b, c) We set $\beta_0\eta/\eta_w = h_0$.

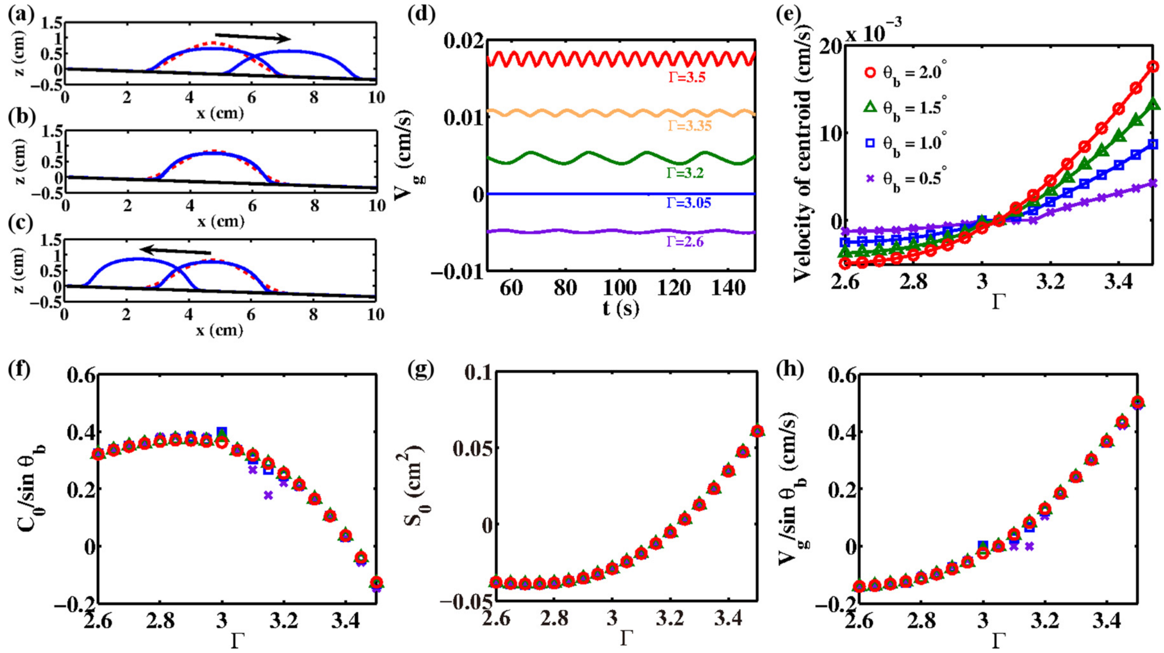

FIG. 7. (Color online) Climbing of a heap. (a–c) The bottom wall is inclined at an angle θ_b from the x axis. The heap (blue line) shows directional motion. The dashed line is the initial condition. $\theta_b = -2^\circ$. (a) $\Gamma = 2.6$. (b) $\Gamma = 3.05$. (c) $\Gamma = 3.2$. (d) Time series of V_g. (e) Velocity of the centroid of a heap. The bottom plate is slightly inclined. A positive velocity indicates that a heap climbs a slope. (f) Dependence of $C_0/\sin\theta_b$ on Γ. (g) Dependence of S_0 on Γ. (h) Dependence of $V_g/\sin\theta_b$ on Γ. (e–h) Purple crosses: $\theta_b = 0.5^\circ$. Blue squares: $\theta_b = 1.0^\circ$. Green triangles: $\theta_b = 1.5^\circ$. Red circles: $\theta_b = 2.0^\circ$. (a–h) $f = 10$ Hz, $\rho = 1$ g/cm^3, $\eta = 100$ St, $\sigma = 72$ dyne/cm, $h_0 = \beta\eta/\eta_w = 0.5$ cm, $B = 10$ Pa, $h_p = 0.005$ cm.

V_g becomes 0 between $\Gamma = 3.0$ and $\Gamma = 3.15$. If we increase the disjoining pressure, the heap adheres to the bottom plate for a wider range of Γ and θ_b. Except at small θ_b, the acceleration at which the heap starts to climb does not depend on θ_b.

Next, we analytically calculate V_g from the time evolution equation of h. We assume a large system and an isolated heap. The system size $2L$ is large compared to the size of a heap. We assume that at a distance from the heap, a flat precursor fluid film covers the bottom plate,

$$h(|x| \gg 1) = h_p \ll 1, \qquad \partial_x h(|x| \gg 1) = 0, \tag{95}$$

where h_p is defined in Appendix C. By using the governing equation [Eq. (60)], the velocity of the centroid x_g is written as

$$\begin{aligned}\partial_t x_g &= \frac{1}{V}\frac{\partial}{\partial t}\int_{-L}^{L} x h(x,t) dx \\ &= \frac{1}{\eta V}\int_{-L}^{L} x\partial_x\left\{\left(\frac{1}{3}h^3 + \frac{\eta}{\eta_w}\beta h^2\right)\partial_x \bar{p}\right\}dx \\ &= \frac{-1}{\eta V}\int_{-L}^{L}\left\{\left(\frac{1}{3}h^3 + \frac{\eta}{\eta_w}\beta h^2\right)\partial_x \bar{p}\right\}dx, \end{aligned}\tag{96}$$

where $V = \int_{-L}^{L} h(x,t)dx$ is the total volume of the fluid. By using the relation $\int_{-L}^{L} h^n \partial_x h dx = 0$, the above equation is reduced to

$$\partial_t x_g = \frac{1}{\eta V}\int_{-L}^{L}\left(\frac{1}{3}h^3 + \frac{\eta}{\eta_w}\beta h^2\right)\left[\sigma\partial_x^3 h + \rho g_h(t)\right]dx. \tag{97}$$

If the bottom plate is inclined, the time-averaged velocity has the form

$$V_g = \frac{1}{T_L}\int_{t_0}^{t_0+T_L}\partial_{t'} x_g dt' = \frac{\sigma}{\eta}C_0 + \frac{\rho g}{\eta}\sin\theta_b S_0, \tag{98}$$

where T_L is large compared to the vibration cycle T. C_0 and S_0 are defined as

$$C_0 = \left\langle \frac{1}{V}\int_{-L}^{L} dx\left(\frac{1}{3}h^3 + \frac{\eta}{\eta_w}\beta h^2\right)\partial_x^3 h\right\rangle_t, \tag{99}$$

$$S_0 = \left\langle \frac{1}{V}\int_{-L}^{L} dx\left(\frac{1}{3}h^3 + \frac{\eta}{\eta_w}\beta h^2\right)\times[-1 + \Gamma\sin(\omega t)]\right\rangle_t, \tag{100}$$

where $\langle\ldots\rangle_t$ is the time average over T_L. Thus, if the motion of the heap reaches a steady state, C_0 and S_0 have constant values and $\langle V_g\rangle_t$ becomes constant. The first term in Eq. (98) comes from the capillary force, and the second term comes from the horizontal gravity. If the horizontal gravity is 0, the steady shape of the heap, h_s, should be symmetric with respect to the peak position of the heap. In this case, $C_0 = 0$ is satisfied. When the horizontal gravity is applied, the shape of the heap deviates from a symmetric shape, $h = h_s + \delta h$. If the inclination angle θ_b is small, so that $g_h \ll 1$, δh should be proportional to $g_h \propto \sin\theta_b$. Because only the integration of the asymmetric part δh has a finite value in Eq. (99), C_0 is expected to be proportional to $\sin\theta_b$. As shown in Fig. 7(f), C_0 is proportional to $\sin\theta_b$, except when the heap adheres to the bottom plate. Because the asymmetric part δh is averaged out in Eq. (100), S_0 is independent of $\sin\theta_b$ [Fig. 7(g)]. Eventually,

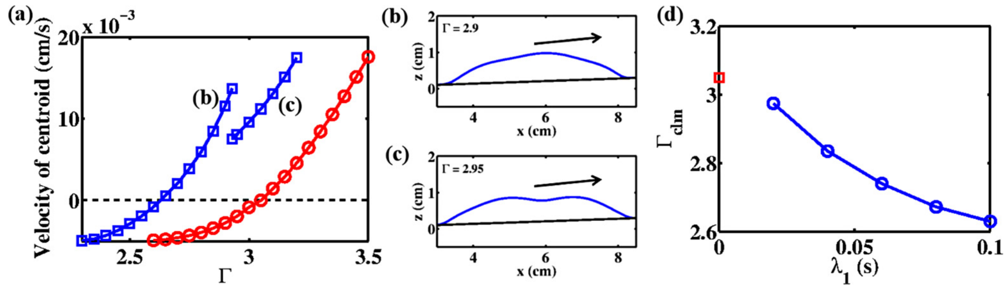

FIG. 8. (Color online) Effect of elasticity on climbing. (a) Velocity of the centroid of a heap. A positive velocity indicates that a heap climbs a slope. Blue squares: velocity of a heap with elasticity. $\lambda_1 = 0.1$ s, $\lambda_2 = 0.01$ s. Red circles: velocity of a heap without elasticity (Newtonian fluid). (b) Steady shape of the heap in faster branch. (c) Steady shape of the heap in slower branch. (d) Blue circles indicate onset acceleration at which heap starts to climb. $\lambda_2 = 0.01$ s. Red square indicates data point of Newtonian fluid. (a–d) $f = 10$ Hz, $\rho = 1$ g/cm^3, $\eta = 100$ St, $\sigma = 72$ dyne/cm, $h_0 = \beta\eta/\eta_w = 0.5$ cm, $B = 10$ Pa, $h_p = 0.005$ cm, $\theta_b = 2^\circ$.

V_g is proportional to $\sin\theta_b$, and $V_g/\sin\theta_b$ converges on a single curve [Fig. 7(h)]. This is why the acceleration at which the heap starts to climb does not depend on the angle of the slope θ_b.

Next, we measure the effect of the elasticity on the climbing speed. We calculate Eq. (58) using Eq. (94). As the relaxation time λ_1 increases, the onset acceleration Γ_{clm} at which the heap starts to climb decreases [Figs. 8(a) and 8(d)]. When the acceleration becomes high, the steady shape of the heap changes discontinuously. At lower acceleration, the heap has one peak [Fig. 8(b)]. At high acceleration, the number of peaks becomes 2, and the climbing velocity suddenly decreases [Fig. 8(c)]. We found that the hysteresis of these two branches is narrow [Fig. 8(a)].

V. DRIFT DUE TO HORIZONTAL VIBRATION

In this section, we consider the case that horizontal vibration is applied onto an isolated heap. We use the same model equation, boundary condition, and initial condition as those in the previous section. Only the gravity and horizontal gravity in Eq. (94) are modified as $g(t) = g[-1 + \Gamma\sin(\omega t)]$ and $g_h(t) = g\Gamma_h\sin(\omega t - \varphi_h)$, where Γ_h and φ_h are the normalized acceleration and phase shift of the horizontal vibration, respectively. Here, we consider only the case that the frequency of horizontal vibration is identical to that of the vertical vibration. The elasticity is not considered. As shown in Fig. 9(a), a heap starts to drift when the horizontal vibration is sufficiently large. The time series of the velocity of the centroid resembles that of a climbing heap [Fig. 7(d)]. The velocity of the centroid is nearly constant but slightly oscillates around a mean value. When the phase shift φ_h is around 0 and 2π, a heap drifts toward a positive direction. On the other hand, around $\varphi_h = \pi$, the heap drifts toward a negative direction. When Γ_h is small or φ_h is around $\pi/2$ and $3\pi/2$, the heap does not drift because of the force from the contact line. For large Γ_h, the front contact line moves faster than the rear [Fig. 9(b)], and the flat liquid layer remains after the droplet.

Next, we briefly checked the drift of a heap in an experiment. For suspensions, we used mixtures of titanium beads and water. The diameter of titanium beads is around 200 μm. We used a narrow acrylic box (10 cm length $\times$ 1 cm width $\times$ 10 cm height) for quasi-2D systems. An initial small heap was subjected to vertical sinusoidal vibration [vertical position $z(t) = A\sin 2\pi f t$] using an electromagnetic vibration system. The motion of the heap was recorded by a high-speed camera. The description of the experimental apparatus is found in Ref. [18]. We simultaneously measured the vibration acceleration along the x, y, and z axis by a time-resolved three-axis acceleration meter. We found that the vibrator had horizontal vibration of x and y directions in addition to the z direction. They can be well fitted by $g\Gamma_i\sin(2\pi f t - \varphi_i)$, $i = x,y$. Γ_i and φ_i depended on the vertical acceleration Γ and vibration frequency f. Because the heap moved only along the long axis of the container, we defined the horizontal vibration along the long axis of the container as $g_h(t) = g\Gamma_h\sin(\omega t - \varphi_h)$. Then, by rotating the acrylic box around the z axis, we varied the horizontal vibration along the long axis of the container, Γ_h. The observed motions of the heap are shown in Figs. 10(a)–10(c). When Γ_h

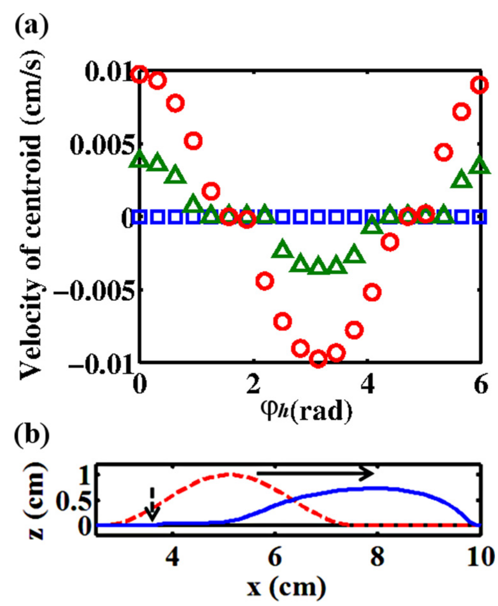

FIG. 9. (Color online) (a) Drift velocity of a heap driven by horizontal vibration. Blue squares: $\Gamma_h = 0.035$. Green triangles: $\Gamma_h = 0.07$. Red circles: $\Gamma_h = 0.14$. (b) Shape of a heap under large horizontal acceleration. $\Gamma_h = 1.00$, $\varphi_h = 0$. Blue solid line: shape of a heap at $t = 32$ s. Red dashed line: initial shape of a heap. Black dashed arrow indicates a position of rear contact line at t=32 s. (a, b) f=10 Hz, ρ=1 g/cm^3, $\eta = 100$ St, $\sigma = 72$ dyne/cm, $h_0 = \beta\eta/\eta_w = 0.5$ cm, $B = 100$ Pa, $h_p = 0.005$ cm.

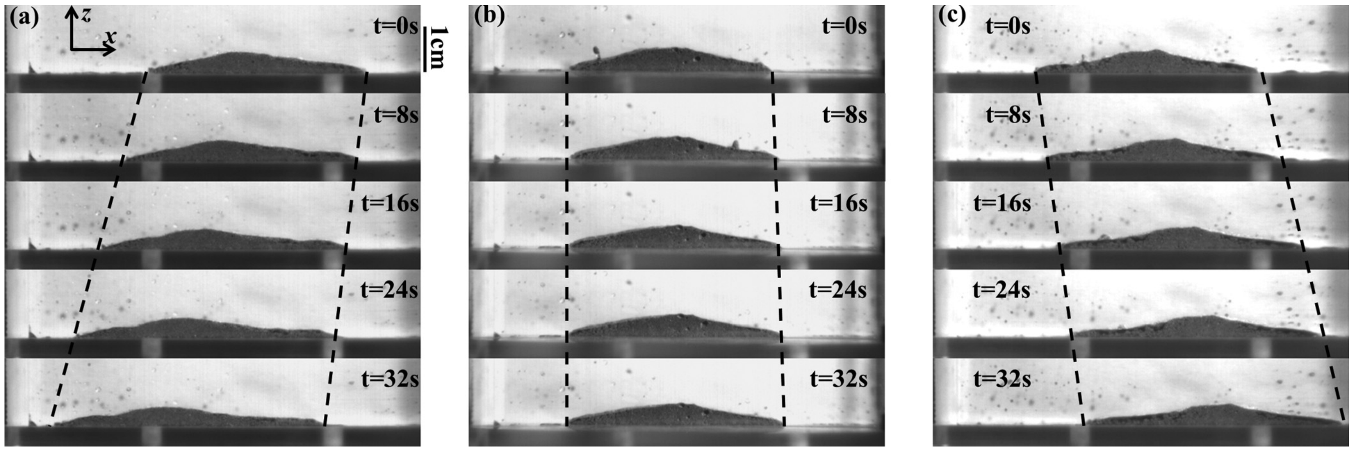

FIG. 10. Drift of a heap in quasi-2D container. Dashed line indicates the position of the contact line. (a) $\Gamma_h = 1.04$, $\varphi_h = 3.62$ rad, $f = 70$ Hz. (b) $\Gamma_h = 0.21$, $\varphi_h = 0.78$ rad, $f = 70$ Hz. (c) $\Gamma_h = 1.26$, $\varphi_h = 5.13$ rad, $f = 80$ Hz. (a–c) $\Gamma = 10.1$. The total volume of the suspension is 1.66 cm^3. The packing fraction of the titanium beads is 58%.

was sufficiently large, a heap drifted with a constant speed, and the front contact line moved faster than the rear [Figs. 10(a) and 10(c)]. Around $\varphi_h = 0$ and 2π, the heap drifted toward a positive direction [Fig. 10(c)]. Around $\varphi_h = \pi$, the heap drifted toward a negative direction [Fig. 10(a)]. If Γ_h was sufficiently small, the heap stuck to the walls and did not move [Fig. 10(b)]. We confirmed that around $\varphi_h = \pi/2$, the heap was almost stationary even for large $\Gamma_h > 1.5$. We varied the frequency from 60 to 100 Hz. Then we obtained the same tendency. This experimental result is in good agreement with our simulation results [Figs. 9(a) and 9(b)]. Compared to the previous work [15] and our simulation (Fig. 9), the accelerations Γ and Γ_h in this experiment are rather large. This is because the heap formation and horizontal drift are strongly suppressed by the narrow geometry. If we used a large container such as a cylindrical container with 10 cm diameter, the horizontal drift was observed with much smaller Γ and Γ_h in our preliminary experiment. Drift due to horizontal vibration is also found for a Newtonian droplet [49]. For the Newtonian droplet, contact line dynamics is crucial for the drift motion. The contact angle of the droplet changes more than 90 deg during one vibration cycle. In our case, a heap drifted even when the change of contact angle was less than 5 deg. Thus, the dynamics of the contact line is expected to have a minor effect. Similar to the drift motion of a dry granular bed on a vibratory conveyor [50–52], we consider that dependence of the slippage on vertical vibration is crucial, as we modeled in Eq. (14).

VI. DISCUSSION AND CONCLUSION

We have proposed a model to explain how the surface of a vibrated dense suspension becomes unstable under a slip-nonslip switching boundary condition [26]. As shown in Figs. 11(a) and 11(b), when gravity acts downward, it generates a flow that relaxes the surface deformation so that the surface becomes flat. On the other hand, when gravity acts upward, it generates a flow that enhances the deformation of the surface, similar to Rayleigh-Taylor instability. Because the time-averaged gravity acts downward, the surface deformation relaxes and the surface becomes flat under an ordinary boundary condition. However, if the boundary condition switches between nonslip and slip, in synchronization with gravity, downward gravity may cause slower flow than upward gravity, depending on the magnitude of the acceleration. The flat surface would then become unstable, similar to Rayleigh-Taylor instability, and steady flow would appear at the boundary. As we show in a weak nonlinear analysis, for a viscous fluid, the rheological characteristics of the bulk fluid are less important, and the boundary condition determines most of the dynamics, especially near the critical point.

We showed that our model can be applied to a viscoelastic fluid if we consider the relaxation and retardation of stress. As we mentioned, synchronization between switching of the boundary condition and gravity is crucial to the surface instability. Thus, the relaxation and retardation of gravitational pressure might prevent the surface instability. However, a small relaxation time does not affect the onset of heap formation. Furthermore, a large relaxation time decreases the onset acceleration of heaping. Thus, a large relaxation time enhances the surface instability. The reason for this decrease in the

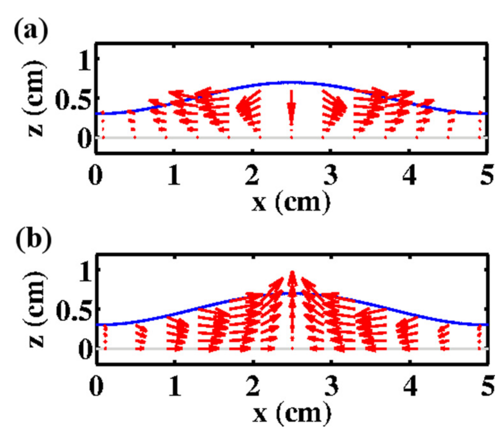

FIG. 11. (Color online) Instantaneous flow field under downward and upward gravity. Blue curve and red arrows indicate surface of the fluid and flow field, respectively. (a) When $g(t) < 0$, velocity is 0 on the bottom. (b) When $g(t) > 0$, velocity is nonzero on the bottom.

onset acceleration can be understood by comparing the time-averaged growth rate of a viscous fluid and that of a viscoelastic fluid. By comparing Eqs. (63) and (85), the time-averaged growth rate of a Maxwell fluid can be expressed as

$$\Lambda_k = \frac{1}{T}\int_0^T dt \frac{k^2}{\eta_{\rm eff}}\left(\frac{1}{3}h_0^3 + \frac{\eta}{\eta_w}\beta h_0^2\right)[\rho g(t) - \sigma k^2], \quad (101)$$

where $\eta_{\rm eff}$ is the effective viscosity of the Maxwell fluid:

$$\eta_{\rm eff} = \eta - \frac{\lambda_1 k^2 h_0^3}{3}[\rho g(t) - \sigma k^2]. \quad (102)$$

The effective viscosity $\eta_{\rm eff}$ is a decreasing function of the gravity $g(t)$. When gravity acts upward, the flow enforces the deformation of the surface. Simultaneously, the viscosity of the Maxwell fluid decreases, so the fluid forms heaps easily. Thus, a large relaxation time decreases the onset acceleration. This effective viscosity is based on linear stability analysis. However, if this shear thinning behavior holds in the nonlinear regime, it also enhances the climbing of the heap. When gravity acts upward, the viscosity decreases so the heap climbs the slope easily.

In this paper, we assume the slip-nonslip switching boundary condition. Ideally, this should be determined by the local dynamics of the granules near the bottom plate. Both in single- and multiparticle systems, bouncing problems on a vibrating surface have been investigated [53–55]. In order to presume a boundary condition in a more realistic manner, we need to understand the detailed behavior of particles in slurry on a vibrating plate. Another important issue is to experimentally confirm the change of the slippage due to the vibration. The slip length is expected to be a function of gap between assembly of granules and a bottom plate. To validate our model, it is required to measure gap size and slip velocity of granules during one vibration cycle.

Our model proposes a mechanism of migration of an isolated domain in addition to surface deformation. For dry granular beds, a combination of vertical and horizontal vibrations causes migration of granules [50,51]. This system is called a vibratory conveyor. The dynamics of granules on a vibratory conveyor is modeled based on the bouncer model [50]. In the model, maximum static frictional force is assumed to be proportional to the gravity $g(t)$, and then slippage depends on the gravity. The model is validated in experiments by measuring the stability and drift speed of a granular bed on the vibratory conveyor [50,52]. Thus, our model could be also tested through the precise measurement of a heap with horizontal vibration.

ACKNOWLEDGMENT

This work was supported by JSPS KAKENHI, Grant-in-Aid No. 25-3349.

APPENDIX A: BOUNCING GRANULAR LAYER

In Eq. (14), we assume that the granular layer touches the bottom plate when gravity acts downward. However, at high vibration frequency, the motion of the granular layer could have a phase delay. In this Appendix, we estimate the necessary condition for Eq. (14) based on the simple model of a bouncing granular layer. We only consider the vertical motion of a granular layer in massless fluid. Similar to previous works, we consider the granular layer as an elastic plug of porosity [35]. In Ref. [35], the motion equation of the granular layer is modeled as the bouncer model with viscous drag force. Here, we introduce the elastic force which comes from the elastic property of a granular layer and free surface. Because the granular layer is surrounded by a viscous fluid, we assume that the collision between the granular layer and the bottom plate is completely inelastic. Then the granular layer stays on the bottom after the collision. When the gravity becomes positive ($\Gamma \sin\omega t > 1$), the granular layer detaches from the bottom plate. Thus, the detaching time t_0 satisfies

$$t_0 = \frac{1}{\omega}\sin^{-1}\left(\frac{1}{\Gamma}\right). \quad (A1)$$

Then the model equations are

$$m\ddot{z} + \gamma_b\dot{z} + k_b z = mg(-1 + \Gamma\sin\omega t), \quad (t_0 \leqslant t \leqslant t_1), \quad (A2)$$

$$z = 0, \qquad \text{otherwise}, \quad (A3)$$

where m, γ_b, and k_b are constant parameters, z is the vertical position of the granular layer measured from bottom plate, and $z = 0$ means that the granular layer is touching on the bottom plate. The granular layer detaches from the bottom plate at $t = t_0$ and touches the bottom plate at $t = t_1$. The terms of the left-hand side in Eq. (A2) are the inertia term, viscous drag force, and elastic force, respectively. The term of the right-hand side is gravity, including the inertial force due to vibration. Here, we consider the strongly dissipative case and neglect the inertia term $m\ddot{z}$. Then the motion equation is

$$\frac{dz}{dT} + \frac{k_b}{\gamma_b\omega}z = \frac{mg}{\gamma_b\omega}(-1 + \Gamma\sin T), \quad (T_0 \leqslant T \leqslant T_1), \quad (A4)$$

where $T = \omega t$. Equation (A4) gives

$$z(T) = \frac{mg}{\gamma_b\omega}e^{-\alpha T}[F(T) - F(T_0)], \quad (A5)$$

$$F(T) = e^{\alpha T}\left\{-\frac{1}{\alpha} + \frac{1}{\alpha^2+1}(\alpha\sin T - \cos T)\right\}, \quad (A6)$$

where $\alpha = k_b/(\gamma_b\omega)$. The touching time T_1 is given by $z(T_1) = 0$, and then $F(T_1) = F(T_0)$. T_1 is numerically calculated as shown in Fig. 12. As α becomes large, T_1 approaches $\pi - T_0$. Note that gravity $g(t)$ changes its sign at $t = (\pi - T_0)/\omega$, $g[(\pi - T_0)/\omega] = 0$. Thus, Eq. (14) is valid when $\alpha \gg 1$. The vibration frequency f must satisfy $f \ll k_b/(2\pi\gamma_b)$. When α is sufficiently small, the grain motion has a phase delay with respect to vibration. This delay has to be taken into account.

APPENDIX B: SCALED CONSTITUTIVE EQUATION

Here we define the scaled deformation rate tensor $\bar{D}_{ij}$ as

$$\bar{D}_{xx} = \epsilon\partial_X U, \quad (B1)$$

$$\bar{D}_{xz} = (\partial_Z U + \epsilon^2\partial_X W)/2, \quad (B2)$$

$$\bar{D}_{zz} = \epsilon\partial_Z W. \quad (B3)$$

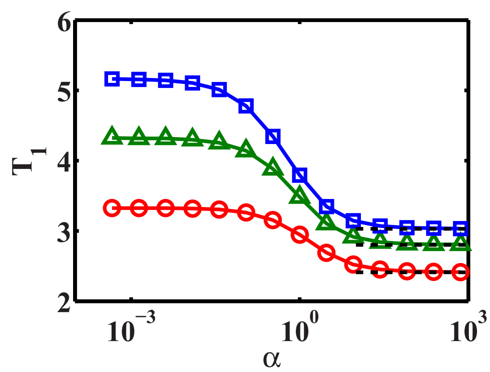

FIG. 12. (Color online) Touching time T_1 as a function of $\alpha = k_b/(\gamma_b\omega)$. Black dashed line indicates $\pi - T_0$. Red circles: $\Gamma = 1.5$. Green triangles: $\Gamma = 3.0$. Blue squares: $\Gamma = 9.0$.

The upper convective derivatives of the shear stress and deformation rate are normalized as

$$\lambda_i \overset{\triangledown}{X}_{xx} = \mathrm{De}_i \partial_T X_{xx} - 2\mathrm{We}_i \partial_Z U X_{xz} + \epsilon \mathrm{We}_i (U \partial_X X_{xx} + W \partial_Z X_{xx} - 2\partial_X U X_{xx}), \quad \text{(B4)}$$

$$\lambda_i \overset{\triangledown}{X}_{xz} = \mathrm{De}_i \partial_T X_{xz} - \mathrm{We}_i \partial_Z U X_{zz} + \epsilon \mathrm{We}_i (U \partial_X X_{xz} + W \partial_Z X_{xz} - \partial_X U X_{xz} - \epsilon \partial_X W X_{xx} - \partial_Z W X_{xz}), \quad \text{(B5)}$$

$$\lambda_i \overset{\triangledown}{X}_{zz} = \mathrm{De}_i \partial_T X_{zz} + \epsilon \mathrm{We}_i (U \partial_X X_{zz} + W \partial_Z X_{zz} - 2\epsilon \partial_X W X_{xz} - 2\partial_Z W X_{zz}), \quad \text{(B6)}$$

where λ_i $(i = 1,2)$ are the relaxation times, and X_{lm} is the scaled shear stress Σ_{lm} and scaled deformation rate $\bar{D}_{lm}$. We_i and De_i $(i = 1,2)$ are the Weissenberg numbers and Deborah numbers, respectively. Then the scaled constitutive equation is

$$\Sigma_{ij} + \lambda_1 \overset{\triangledown}{\Sigma}_{ij} = 2(\bar{D}_{ij} + \lambda_2 \overset{\triangledown}{\bar{D}}_{ij}), \quad \text{(B7)}$$

where $i,j = x,z$.

APPENDIX C: CONTACT LINE

If a completely dry region $h = 0$ appears, we have to consider the contact line. Here we use the disjoining pressure ψ to avoid complete dewetting and treat the contact line without a singularity [42,56],

$$\psi = B\left[\left(\frac{h_p}{h}\right)^3 - \left(\frac{h_p}{h}\right)^4\right], \quad \text{(C1)}$$

where h_p is the thickness of the precursor layer. The disjoining pressure contains intermolecular attractive and repulsive forces. The local disjoining energy has a minimum at h_p. In this model, we assume that a very thin precursor fluid layer spreads out around the contact line, and the bottom plate is always covered by the fluid. The thickness of the precursor layer h_p is set to be larger than that in the experimental result because of a computational limitation [57]. The equilibrium contact angle θ_e is given by the following relation [56]:

$$B = \frac{6\sigma}{h_p}(1 - \cos\theta_e). \quad \text{(C2)}$$

When we introduce the disjoining pressure, the reduced pressure [Eq. (48)] is modified as

$$\bar{p} = -\left[\rho g(t) + \sigma\left(\partial_x^2 + \partial_y^2\right)\right]h + \psi. \quad \text{(C3)}$$

APPENDIX D: WEAK NONLINEAR ANALYSIS

In this Appendix, we derive h_1, h_2, M, α, and γ. From Eqs. (71) and (72), $\hat{h}_1$ satisfies

$$\partial_t \hat{h}_1 - \left(\frac{1}{3}h_0^3 + \beta h_0^2\right)\Pi(k_m)\hat{h}_1 = 0, \quad \text{(D1)}$$

$$\Pi(k) = \frac{k^2}{\eta_0}[\rho g_c(t) - \sigma k^2]. \quad \text{(D2)}$$

As a result, $\hat{h}_1$ is solved as

$$\hat{h}_1 = \exp\left\{\int_0^t dt\left(\frac{1}{3}h_0^3 + \beta h_0^2\right)\Pi(k_m)\right\}. \quad \text{(D3)}$$

From Eqs. (74) and (75), the equation for $\hat{h}_2$ is obtained as

$$\partial_t \hat{h}_2 - \left(\tfrac{1}{3}h_0^3 + \beta h_0^2\right)\Pi(2k_m)\hat{h}_2 = 2\left(h_0^2 + 2\beta h_0\right)\Pi(k_m)\hat{h}_1^2. \quad \text{(D4)}$$

To make the calculation clear, we introduce following variables:

$$S(t) = \left(\tfrac{1}{3}h_0^3 + \beta h_0^2\right)\Pi(2k_m), \quad \text{(D5)}$$

$$R(t) = 2\left(h_0^2 + 2\beta h_0\right)\Pi(k_m)\hat{h}_1^2. \quad \text{(D6)}$$

$\hat{h}_2$ has a time-periodic part (particular solution) and a relaxing part (general solution). The relaxing part is less important, and we ignore it. The time-periodic part is calculated if we apply the condition $\hat{h}_2(nT) = \hat{h}_2[(n-1)T]$. Then, $\hat{h}_2$ is

$$\hat{h}_2(t) = \exp\left(\int_0^t dt S(t)\right)\left\{I_t + \int_0^t dt' R(t') \exp\left(-\int_0^{t'} dt'' S(t'')\right)\right\}. \tag{D7}$$

I_t is defined as follows:

$$I_t = \frac{\exp(\zeta T)}{1-\exp(\zeta T)} \int_0^T dt' R(t') \exp\left(-\int_0^{t'} dt'' S(t'')\right), \tag{D8}$$

$$\zeta = -\frac{6k_m^4 h_0^3 \sigma}{\pi \eta_0} \int_0^{2\pi} dx \left(\frac{1}{3} + \frac{\beta(x)}{h_0}\right). \tag{D9}$$

The equation of $O(\epsilon_2^3)$ becomes

$$\mathbf{L}_0 h_3 = M, \tag{D10}$$

where M is defined as

$$\begin{aligned} M = &-\partial_\tau A \hat{h}_1 + \eta_0^{-1} k_m^2 \frac{\partial \beta}{\partial \Gamma} h_0^2 \chi \Gamma_c \Pi(k_m) \hat{h}_1 A + \eta_0^{-1} k_m^2 \left(\frac{1}{3} h_0^3 + \beta h_0^2\right) \rho g \chi \Gamma_c \sin(\omega t) \hat{h}_1 A + \frac{1}{2}\left(h_0^2 + 2\beta h_0\right) \Pi(2k_m) \hat{h}_2 \hat{h}_1 A |A|^2 \\ &-\left(h_0^2 + 2\beta h_0\right) \Pi(k_m) \hat{h}_2 \hat{h}_1 A |A|^2 + (h_0 + \beta) \Pi(k_m) \hat{h}_1^3 A |A|^2 - \frac{3\eta_0 h_0^5}{5k_m^2} \frac{\partial^2 \eta(0)}{\partial \tau_{xz}^2} [\Pi(k_m) \hat{h}_1]^3 A |A|^2. \end{aligned} \tag{D11}$$

The solvability condition requires that M is orthogonal to $\hat{h}_1$,

$$\frac{1}{T} \int_0^T dt \hat{h}_1^{-1} M = 0. \tag{D12}$$

Then we obtain the evolution equation of A,

$$\partial_\tau A = \alpha A + \gamma A |A|^2, \tag{D13}$$

where α and γ are

$$\alpha = \frac{1}{T} \int_0^T dt \ \chi \Gamma_c \left\{\frac{\partial \beta}{\partial \Gamma} h_0^2 \Pi(k_m) + \left(\frac{1}{3} h_0^3 + \beta h_0^2\right) k_m^2 \frac{\rho g}{\eta_0} \sin(\omega t)\right\}, \tag{D14}$$

$$\gamma = \frac{1}{T} \int_0^T dt \ \left\{\frac{1}{2}\left(h_0^2 + 2\beta h_0\right) \Pi(2k_m) \hat{h}_2 - \left(h_0^2 + 2\beta h_0\right) \Pi(k_m) \hat{h}_2 + (h_0 + \beta) \Pi(k_m) \hat{h}_1^2 - \frac{3\eta_0 h_0^5}{5k_m^2} \frac{\partial^2 \eta(0)}{\partial \tau_{xz}^2} [\Pi(k_m)]^3 \hat{h}_1^2\right\}. \tag{D15}$$

[1] Lord Rayleigh, On the instability of jets, Proc. Lond. Math. Soc. **s1-10**, 4 (1878).

[2] C. L. Shen, W. J. Xie, and B. Wei, Parametrically excited sectorial oscillation of liquid drops floating in ultrasound, Phys. Rev. E **81**, 046305 (2010).

[3] Y. Fautrelle, J. Etay, and S. Daugan, Free-surface horizontal waves generated by low-frequency alternating magnetic fields, J. Fluid Mech. **527**, 285 (2005).

[4] P. Brunet and J. H. Snoeijer, Star-drops formed by periodic excitation and on an air cushion—A short review, Eur. Phys. J.: Spec. Top. **192**, 207 (2011).

[5] G. I. Taylor, The instability of liquid surface when accelerated in a direction perpendicular to their planes (I), Proc. R. Soc. London A **201**, 192 (1950).

[6] R. D. Richtmyer, Taylor instability in shock acceleration of compressible fluids, Commun. Pure Appl. Math. **13**, 297 (1960).

[7] E. E. Meshkov, Instability of the interface of two gases accelerated by a shock wave, Fluid Dyn. **4**, 101 (1969).

[8] M. Faraday, On a peculiar class of acoustical figures; and on certain forms assumed by a group of particles upon vibrating elastic surfaces, Philos. Trans. R. Soc. London **121**, 299 (1831).

[9] I. S. Fayzrakhmanova and A. V. Straube, Stick-slip dynamics of an oscillated sessile drop, Phys. Fluids **21**, 072104 (2009).

[10] O. Manor, M. Dentry, J. R. Friend, and L. Y. Yeo, Substrate dependent drop deformation and wetting under high frequency vibration, Soft Matter **7**, 7976 (2011).

[11] A. R. Rezk, O. Manor, J. R. Friend, and L. Y. Yeo, Unique fingering instabilities and soliton-like wave propagation in thin acoustowetting films, Nat. Commun. **3**, 1167 (2012).

[12] O. Manor, Diminution of contact angle hysteresis under the influence of an oscillating force, Langmuir **30**, 6841 (2014).

[13] A. R. Rezk, O. Manor, L. Y. Yeo, and J. R. Friend, Double flow reversal in thin liquid films driven by megahertz-order surface vibration, Proc. R. Soc. A **470**, 20130765 (2014).

[14] R. G. Larson, Instabilities in viscoelastic flows, Rheol. Acta **31**, 213 (1992).

[15] J. M. Schleier-Smith and H. A. Stone, Convection, Heaping, and Cracking in Vertically Vibrated Granular Slurries, Phys. Rev. Lett. **86**, 3016 (2001).

[16] F. Merkt, R. D. Deegan, D. Goldman, E. Rericha, and H. L. Swinney, Persistent Holes in a Fluid, Phys. Rev. Lett. **92**, 184501 (2004).
[17] H. Ebata and M. Sano, Self-Replicating Holes in a Vertically Vibrated Dense Suspension, Phys. Rev. Lett. **107**, 088301 (2011).
[18] H. Ebata, S. Tatsumi, and M. Sano, Expanding holes driven by convectionlike flow in vibrated dense suspensions, Phys. Rev. E **79**, 066308 (2009).
[19] Y. Xu, X. Gong, Y. Sun, S. Xuan, W. Jiang, and Z. Zhang, Evolution of the initial hole in vertically vibrated shear thickening fluids, Phys. Rev. E **83**, 056311 (2011).
[20] R. D. Deegan, Stress hysteresis as the cause of persistent holes in particulate suspensions, Phys. Rev. E **81**, 036319 (2010).
[21] H. Ebata and M. Sano, Bifurcation from stable holes to replicating holes in vibrated dense suspensions, Phys. Rev. E **88**, 053007 (2013).
[22] S. von Kann, J. H. Snoeijer, and D. van der Meer, Phase diagram of vertically vibrated dense suspensions, Phys. Fluids **26**, 113302 (2014).
[23] C. Falcón, J. Bruggeman, M. Pasquali, and R. D. Deegan, Localized structures in vibrated emulsions, Europhys. Lett. **98**, 24002 (2012).
[24] J. M. Wolf, S. R. Dungan, M. J. McCarthy, V. Lim, and R. J. Phillips, Vibration-induced geometric patterns of persistent holes in Carbopol gels, J. Non-Newtonian Fluid Mech. **220**, 99 (2015).
[25] H. Shiba, J. E. Ruppert-Felsot, Y. Takahashi, Y. Murayama, Q. Ouyang, and M. Sano, Elastic Convection in Vibrated Viscoplastic Fluids, Phys. Rev. Lett. **98**, 044501 (2007).
[26] H. Ebata and M. Sano, Heaps in the fluid film induced by slip-nonslip switching boundary condition, Europhys. Lett. **100**, 14001 (2012).
[27] P. Evesque and J. Rajchenbach, Instability in a Sand Heap, Phys. Rev. Lett. **62**, 44 (1989).
[28] J. Duran, Ripples in Tapped or Blown Powder, Phys. Rev. Lett. **84**, 5126 (2000).
[29] J. Duran, Rayleigh-Taylor Instabilities in Thin Films of Tapped Powder, Phys. Rev. Lett. **87**, 254301 (2001).
[30] H. K. Pak, E. Van Doorn, and R. P. Behringer, Effects of Ambient Gases on Granular Materials under Vertical Vibration, Phys. Rev. Lett. **74**, 4643 (1995).
[31] B. Thomas and A. M. Squires, Support for Faraday's View of Circulation in a Fine-Powder Chladni Heap, Phys. Rev. Lett. **81**, 574 (1998).
[32] E. Clément, J. Duran, and J. Rajchenbach, Experimental Study of Heaping in a Two-Dimensional "Sand Pile", Phys. Rev. Lett. **69**, 1189 (1992).
[33] J. Lee, Heap formation in two-dimensional granular media, J. Phys. A: Math. Gen. **27**, L257 (1994).
[34] R. J. Milburn, M. A. Naylor, A. J. Smith, M. C. Leaper, K. Good, M. R. Swift, and P. J. King, Faraday tilting of water-immersed granular beds, Phys. Rev. E **71**, 011308 (2005).
[35] P. J. King, P. Lopez-Alcaraz, H. A. Pacheco-Martinez, C. P. Clement, A. J. Smith, and M. R. Swift, Instabilities in vertically vibrated fluid-grain systems, Eur. Phys. J. E **22**, 219 (2007).
[36] I. Cohen, B. Davidovitch, A. B. Schofield, M. P. Brenner, and D. A. Weitz, Slip, Yield, and Bands in Colloidal Crystals under Oscillatory Shear, Phys. Rev. Lett. **97**, 215502 (2006).
[37] P. Ballesta, R. Besseling, L. Isa, G. Petekidis, and W. C. K. Poon, Slip and Flow of Hard-Sphere Colloidal Glasses, Phys. Rev. Lett. **101**, 258301 (2008).
[38] L. Chen, Y. Duan, M. Liu, and C. Zhao, Slip flow of coal water slurries in pipelines, Fuel **89**, 1119 (2010).
[39] P. S. Hammond, Nonlinear adjustment of a thin annular film of viscous fluid surrounding a thread of another within a circular cylindrical pipe, J. Fluid Mech. **137**, 363 (1983).
[40] S. G. Yiantsios and B. G. Higgins, Rayleigh-Taylor instability in thin viscous films, Phys. Fluids A **1**, 1484 (1989).
[41] M. Fermigier, L. Limat, J. E. Wesfreid, P. Boudinet, and C. Quilliet, Two-dimensional patterns in Rayleigh-Taylor instability of a thin layer, J. Fluid Mech. **236**, 349 (1992).
[42] A. Oron, S. H. Davis, and S. G. Bankoff, Long-scale evolution of thin liquid films, Rev. Mod. Phys. **69**, 931 (1997).
[43] C. Hanotin, S. Kiesgen de Richter, P. Marchal, L. J. Michot, and C. Baravian, Vibration-Induced Liquefaction of Granular Suspensions, Phys. Rev. Lett. **108**, 198301 (2012).
[44] Ph. Marchal, C. Hanotin, L. J. Michot, and S. Kiesgen de Richter, Two-state model to describe the rheological behavior of vibrated granular matter, Phys. Rev. E **88**, 012207 (2013).
[45] C. Hanotin, S. Kiesgen de Richter, L. J. Michot, and Ph. Marchal, Viscoelasticity of vibrated granular suspensions, J. Rheol. **59**, 253 (2015).
[46] E. A. Cerda and E. L. Tirapegui, Faraday's instability in viscous fluid, J. Fluid Mech. **368**, 195 (1998).
[47] Y. Kuramoto, *Chemical Oscillations, Waves, and Turbulence* (Springer-Verlag, Berlin, 1984).
[48] P. Brunet, J. Eggers, and R. D. Deegan, Vibration-Induced Climbing of Drops, Phys. Rev. Lett. **99**, 144501 (2007).
[49] X. Noblin, R. Kofman, and F. Celestini, Ratchetlike Motion of a Shaken Drop, Phys. Rev. Lett. **102**, 194504 (2009).
[50] E. M. Sloot and N. P. Kruyt, Theoretical and experimental study of the transport of granular materials by inclined vibratory conveyors, Powder Technol. **87**, 203 (1996).
[51] R. Grochowski, P. Walzel, M. Rouijaa, C. A. Kruelle, and I. Rehberg, Reversing Granular Flow on a Vibratory Conveyor, Appl. Phys. Lett. **84**, 1019 (2004).
[52] P. J. King, M. R. Swift, K. A. Benedict, and A. Routledge, Surface stability of granular systems under horizontal and vertical vibration: The applicability of a coefficient of friction, Phys. Rev. E **62**, 6982 (2000).
[53] J. J. Barroso, M. V. Carneiro, and E. E. N. Macau, Bouncing ball problem: Stability of the periodic modes, Phys. Rev. E **79**, 026206 (2009).
[54] S. Luding, E. Clément, A. Blumen, J. Rajchenbach, and J. Duran, Studies of columns of beads under external vibrations, Phys. Rev. E **49**, 1634 (1994).
[55] P. Eshuis, K. van der Weele, D. van der Meer, and D. Lohse, Granular Leidenfrost Effect: Experiment and Theory of Floating Particle Clusters, Phys. Rev. Lett. **95**, 258001 (2005).
[56] L. W. Schwartz, Hysteretic effects in droplet motions on heterogeneous substrates: Direct numerical simulation, Langmuir **14**, 3440 (1998).
[57] S. B. G. O'Brien and L. W. Schwartz, *Encyclopedia of Surface and Colloid Science* (Dekker, New York, 2002), p. 5283.